Journal of Computational Physics 231 (2012) 8262–8277

Contents lists available at SciVerse ScienceDirect

Journal of Computational Physics

journal homepage: www.elsevier.com/locate/jcp

Propagation of ocean surface waves on a spherical multiple-cell grid

Jian-Guo Li *

Met Office, FitzRoy Road, Exeter EX1 3PB, United Kingdom

ARTICLE INFO

Article history:
Received 28 November 2011
Received in revised form 28 June 2012
Accepted 3 August 2012
Available online 16 August 2012

Keywords:
Ocean surface wave
Global transport
Wave spectrum
Polar problem
Unstructured grid
Wave refraction

ABSTRACT

Satellite observations have established that the Arctic ice is retreating faster than expected and global ocean surface wave models have to be extended to cover the polar region in the future. The major obstacle preventing the wave model extension is that the diminishing longitude grid-length at high latitudes exerts a severe restriction on time steps and leads to polar singularity. A spherical multiple-cell (SMC) grid is installed in a global wave model to overcome the polar problems. A 2nd order upstream non-oscillatory advection scheme and a rotation scheme for wave spectral refraction are used. The unstructured SMC grid allows time step to be relaxed and land cells to be removed, saving over 1/3 of the total computation time in comparison with the original latitude–longitude grid model. It also allows multi-resolutions within one model domain so that coastlines and small islands can be resolved at refined resolutions. It also makes it possible to merge regional models into a single global model, replacing nested models in operational forecasting systems. Validations with satellite and buoy observations show that the SMC grid wave model performs as well as the latitude–longitude grid model and yields better swell predictions if coastlines and small islands are resolved at refined resolutions. Due to the ice coverage in the Arctic, an ideal wave spectral propagation in an ice-free Arctic is used to illustrate a map-east reference direction method for extension of the wave model over the whole Arctic.

© 2012 Elsevier Inc. All rights reserved.

1. Introduction

Satellite and in situ observations of global ice coverage have revealed that glaciers at high altitudes and sea ice at high latitudes are retreating at alarming speeds and an essentially ice-free Arctic summer is 'expected' in the future [46]. The ice coverage in the Arctic shrunk as high as 86°N in summer 2007, opening new shipping routes cross the Arctic and calling ocean surface wave models to extend at high latitudes. The unprecedented Arctic sea ice retreat in summer 2007 is believed to be driven by warmed ocean currents [32], increased melt and enhanced transpolar wind drift of sea ice [50]. It seems to be only a matter of time before the whole Arctic ocean has to be included in global ocean surface wave models.

The major problem to extend a latitude–longitude (lat–lon) grid wave model at high latitudes is the diminishing longitude grid-length towards the Pole, which exerts a severe restriction on time steps of finite-difference schemes (advection and diffusion in particular). Another problem is the increased curvature of the parallels at high latitudes. The rapid change of the local east direction renders the scalar assumption invalid for any vector component defined relative to the local east direction. In ocean surface wave models [45,5,43], the wave energy spectrum is discretised into directional components relative to the local east. Each directional component is treated as a scalar, that is, the corresponding spectral components in neighbouring cells are assumed to be at the same direction. This scalar assumption is a good approximation outside the polar

* Tel.: +44 1392 884885; fax: +44 1392 885681.
E-mail address: Jian-Guo.Li@metoffice.gov.uk

0021-9991/$ - see front matter © 2012 Elsevier Inc. All rights reserved.
http://dx.doi.org/10.1016/j.jcp.2012.08.007

region; however, it becomes erroneous at high latitudes since the change of direction over one longitude grid length grows too large to be ignored if a reduced grid is used.

Special grids have been developed to tackle the polar problems in geo-fluid dynamics [47] and some of them have found their applications in ocean surface wave models, such as the curvilinear grid [36] and the unstructured finite-element grid [37]. The spherical multiple-cell (SMC) grid [23] is an efficient approach and has been validated with classic numerical tests [48,29]. The SMC grid has the flexibility to remove all land points out of the wave propagation schemes and requires minimal changes to the lat–lon grid finite-difference schemes because the lat–lon "rectangular" cells are retained. The multiple-cell grid is first developed for air pollution modelling [21], originated from the one-side flux approach [24] and an ocean model work [18]. The SMC grid relaxes the Courant–Friedrichs–Lewy (CFL) restriction of the Eulerian advection time-step by merging longitudinal cells towards the Poles as in the reduced grid [34]. Round polar cells are introduced to remove the polar singularity of the spherical coordinate system. Vector component propagation errors caused by the scalar assumption at high latitude is removed by replacing the local east with a fixed reference direction, for instance, the map-east as viewed in a polar stereographic projection, to define the wave spectral components in the Arctic.

Besides, unresolved small islands are incurring errors in global ocean surface wave models as they are important sinks of the ocean surface wave energy [41]. Missed island groups in coarse resolution global models lead to a persistent under-prediction of wave energy blocking [49]. Although the far field errors can be alleviated with sub-grid obstructions, high resolution around islands is still the most appropriate approach for accurate swell prediction close to islands [7]. Near-shore bathymetry features also contribute to some non-linear wave features, like freak waves [16]. Nested grids with two-way interactions [42], adaptive mesh refinement grid [33], and finite-element grid [37] have been installed in wave models for refined resolutions near coastlines or in interested regions. One feature of the unstructured SMC grid is that it can also handle multiple resolutions within the same model so that small islands and coastlines are resolved at high resolutions while the vast open oceans are kept at an affordable resolution. This is a very appealing option for operational models as increasing resolution throughout the full model domain to resolve small islands is not economical. The feature also allows regional models to be merged into one global model, an option to be exploited in future studies.

This paper will show the implementation of the SMC grid in a global ocean surface wave model, which is adapted from the WAVEWATCH III model [38,43]. The multi-resolution feature is illustrated with a 3-level multi-resolution grid. Satellite altimeter and buoy wave observations are used for validation of the SMC grid model and comparison with the original lat–lon grid model. Because the ice cover in the Arctic prevents testing of the extension over the whole Arctic, an idealised ocean wave spectral propagation in an ice-free Arctic is used to demonstrate the map-east reference direction method.

2. Wave propagation on a sphere

The Eulerian ocean surface wave model is based on a 2-D spectral energy balance equation. In the 2-D spherical coordinates with longitude λ and latitude φ, the equation is given by

$$\frac{\partial\psi}{\partial t} + \frac{\partial F_x}{\partial x} + \frac{\partial(F_y\cos\varphi)}{\cos\varphi\partial y} + \frac{\partial(\dot{k}\psi)}{\partial k} + \frac{\partial(\dot{\theta}\psi)}{\partial\theta} = S$$

$$F_x \equiv u\psi - D_x\partial\psi/\partial x,\ F_y \equiv \upsilon\psi - D_y\partial\psi/\partial y \tag{1}$$

where $\psi(t,\lambda,\varphi,k,\theta)$ is any component of the wave energy spectrum, t is the time, k is the wave number, θ is the spectral direction usually defined from the local east direction, u and υ are the zonal and meridian components of the wave energy propagation speed, D_x and D_y are the diffusion coefficients, and S the source term. The geophysical coordinates x and y are defined locally eastward along the parallel and northward along the meridian, respectively. So their increments are given by $dx = r\cos\varphi d\lambda$, $dy = rd\varphi$, where r is the radius of the sphere. The overhead dot indicates time differentiation along the wave propagation path. The r.h.s S represents all source terms. This study uses an adapted version of the WAVEWATCH III model [43,38] and its source terms are unchanged from the original model [44,12]. Note that in WAVEWATCH III model the wave action $A \equiv \psi/\omega$, where ω is the intrinsic angular frequency of the ocean surface wave, is chosen instead of the wave energy ψ for conservation when ocean current is present. The wave action shares the same equation (1) as the wave energy except that the source term is divided by ω. Hence all propagation schemes for wave energy can be applied on wave action.

The spherical wave energy balance equation (1) differs from its Cartesian counterpart in the meridian differential term by an extra cosine factor, which renders the term undefined (singular) at the Poles. Thus, except for at the Poles, Eq. (1) can be approximated with finite-difference schemes similar to those used in the Cartesian grid. The only difference between the Cartesian and spherical versions of these finite-difference schemes is that the latter has an extra cosine factor. Because the SMC grid retains the lat–lon grid cells, the wave energy balance equation (1) is also valid on the SMC grid.

The diffusion term in (1) may be considered as the sub-grid mixing term as in atmospheric models [31] because the model wave spectrum represents the spatial average over one grid cell. This diffusion term is usually parameterised to alleviate the so called garden-sprinkler effect (GSE) due to discretization of the wave energy spectrum [4,40,1]. In old wave models the explicit diffusion term was also used for suppression of numerical oscillations caused by other terms [49].

One primary physical process that affects surface wave propagation is the depth-induced refraction [28]. Refraction formulations in contemporary surface wave models are based on the linear theory, assuming slow-varying ocean depth, which leads to the following surface wave dispersion relationship [3]:

$$\omega^2 = gk\tanh(kh) \tag{2}$$

For a given intrinsic angular frequency ω, the wave number k varies with water depth h and can be determined by the iteration $k_{i+1} = 1/(h_g \tanh(hk_i))$, starting with $k_0 = 1/h_g$, where $i = 0, 1, 2 \ldots$ is the iteration number and $h_g = g/\omega^2$ will be referred to as the *gravity depth*. A fitting function with the dimensionless variable h/h_g is also available for estimation of the wave number [9].

Phillips [30] derived the surface wave ray equation from the dispersion relationship (2) and the following kinematical conservation equation:

$$\partial\mathbf{k}/\partial t + \nabla(\omega + \mathbf{k}\cdot\mathbf{U}) = 0 \tag{3}$$

where $\mathbf{k} = (k\cos\theta, k\sin\theta)$ is the wave number vector, ∇ is the 2-D gradient operator, and $\mathbf{U}$ is the ambient current velocity. Inserting the dispersion relationship (2) into (3), we have

$$\partial\mathbf{k}/\partial t + (c_g + U_k)\nabla k + \xi k\nabla h + k\nabla U_k = 0 \tag{4}$$

where $U_k = \mathbf{k}\cdot\mathbf{U}/k$ is the ambient current velocity component along the $\mathbf{k}$ direction, $\xi = \omega/\sinh(2kh)$ will be referred to as the *refraction factor*, and c_g is the wave group speed defined by

$$c_g = \partial\omega/\partial k = c_{gd}(\tanh(kh) + kh/\cosh^2(kh)) \tag{5}$$

in which $c_{gd} = g/2\omega$ is the group speed in deep waters ($h >> h_g$). Surface wave energy travels at the group speed rather than the phase speed $c = \omega/k$. Note that the group speed (5) is not a monotonic function of the water depth as illustrated in Fig. 1. As waves move towards shallow waters, the group speed increases and reaches a maximum, $c_{gm} = \beta_m c_{gd}$, when the water depth decreases to the gravity depth h_g. The factor $\beta_m \sim 1.19968$ is the root of $\beta\tanh\beta = 1$. After the peak speed, wave group speed starts to decrease with water depth and can be approximated by $c_{gs} = \sqrt{gh}$ in shallow waters ($h << h_g$).

Note that the gravity depth is a function of wave frequency so shallowness is a relative description of surface waves. For wind waves, the frequency range is from about 0.04 to 0.4 Hz, which results in a gravity depth ranging from 155 to 1.55 m. So oceans over a few of hundreds meters in depth are considered deep for wind-induced waves. For tsunami waves, however, the entire world oceans are shallow because tsunami frequency is extremely small. It can be worked out from Fig. 1 that the group speed exceeds the deep water speed in the region from roughly $h_g/3$ to $3h_g$. So it would be practical to say that, for a given surface wave frequency, the water is deep if $h > 3h_g$ or shallow if $h < h_g/3$. This definition is simpler than the conventional definition based on the value of kh (see [13,16] for instance), because k also varies with depth. The gravity depth h_g is a constant for a given intrinsic frequency and hence a practical depth scale to define shallow and deep waters.

Phillips [30] assumed a steady wave train ($\partial\mathbf{k}/\partial t = 0$) in (4) to derive the following wave ray equations:

$$(c_g + U_k)\partial k/\partial s = -\xi\mathbf{k}\cdot\nabla h - \mathbf{k}\cdot\nabla U_k, \quad (c_g + U_k)\partial\theta/\partial s = -\xi\mathbf{n}\cdot\nabla h - \mathbf{n}\cdot\nabla U_k \tag{6}$$

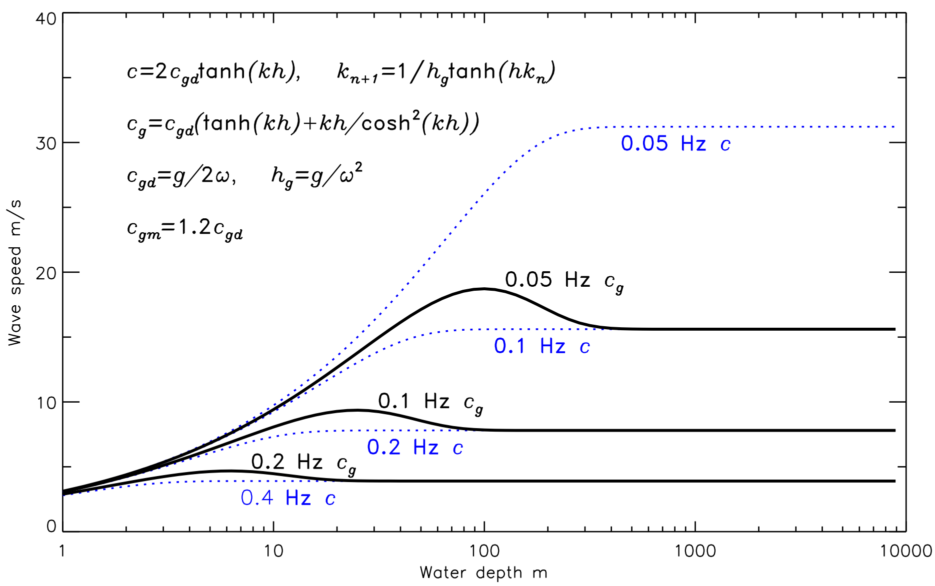

Fig. 1. Variations of ocean surface wave speed with water depth.

where s is the distance along the wave path at the $\mathbf{k}$ or θ direction and $\mathbf{n} = (-\sin\theta, \cos\theta)$ is a unit vector normal to the $\mathbf{k}$ direction to the left or at $\theta + \pi/2$. Note that the wave energy propagation speed at the $\mathbf{k}$ direction in the presence of an ambient current is $c_g + U_k$, the time changing rate of the wave number and its direction along the wave path are then given by

$$\dot{k} = -\xi \mathbf{k} \cdot \nabla h - \mathbf{k} \cdot \nabla U_k \tag{7a}$$

$$\dot{\theta}_{rfr} = -\xi \mathbf{n} \cdot \nabla h - \mathbf{n} \cdot \nabla U_k \tag{7b}$$

The direction change rate (7b) is called the refraction rate and can also be derived in analogy to the Snell's law in geometrical optics [26,19,14]. The simplicity of the optical refraction theory makes it ideal for operational models. Magne et al. [27] compared an optical refraction model and some more complicated models with observations in step ocean canyons, near San Diego, California and concluded that the simple refraction model is in good agreement with observations and very robust even over wide range of depth gradients.

Wave energy travels along the shortest route on the ocean surface, that is, along great circles on the sphere. So a wave spectral component will not be confined at its defined direction but will shift gradually with latitude along its great circle path, a procedure known as great circle turning (GCT). Assuming the great circle direction is at an angle θ from the local east direction at latitude φ, the product of cosines of these two angles is conserved on the great circle path, that is, $\cos\theta \cos\varphi = const.$, which provides a simple rule for navigation along great circles and leads to the following GCT rate along the propagation direction

$$\dot{\theta}_{gct} = -(c_g/r)\cos\theta \tan\varphi \tag{8}$$

The net wave direction changing rate used in (1) is then the sum of the refraction rate (7b) and the GCT rate (8).

3. Numerical schemes on a SMC grid

Scalar advection schemes on the SMC grid are described in [23]. Here summarised are other terms in (1) and treatment of advection and diffusion on multi-resolution SMC grid. It also tackles the polar problem with vector components at high latitudes.

3.1. Advection–diffusion schemes

A global SMC grid is shown in Fig. 2. For clarity, only the Arctic region is shown here. The base resolution of the SMC grid is set to be equal to the horizontal resolution of the Met Office weather forecast model, which provides the marine surface wind. The lat–lon grid of the forecast model is at the resolution of $\Delta\lambda = 360°/1024 = 0.3515625°$ and $\Delta\varphi = 180°/768 = 0.234375°$ and the latitudinal grid length is about 25 km. The SMC grid uses only the sea points or cells and refines the resolution by two levels to 6 km around islands and coastlines, resulting in a global 3-level (6-12-25 km) SMC grid on ocean surface. This SMC grid will be referred to as the SMC6-25 grid. Cells are merged longitudinally at high latitudes following the same rules in [23] to relax the CFL restriction. A unique 5-element integer array is assigned to each cell to hold its x, y grid indices, cell x/y-sizes, and water depth. The cells are listed as a 1-D array and sorted by their y-size for use of sub-time steps on refined cells. The cell array is used for propagation schemes and input/output mapping.

The l.h.s terms in (1) are calculated with time-splitting approaches by combining the first (time differential) term with each of the other 4 terms. The advection-diffusion terms are discretised on the SMC grid with one flux loop and one cell loop for each dimension. Cell faces are named by its normal velocity components as u- or v-faces. An 8-element integer array is pre-calculated for each face to store its face position, size, and its upstream-central-downstream (UCD) cell indices. This face array is used to calculate its advection-diffusion flux and the depth gradient.

Note that the diffusion term used here is slightly different from the original GSE smoothing term [4]. The original diffusion term is designed to enhance the transverse smoothing because a first order upstream advection scheme is used and it has already introduced strong smoothing along the wave propagation direction. The asymmetrical diffusion results in a cross term in Cartesian coordinates [4]. In this SMC grid wave model, the advection is estimated with an upstream non-oscillatory 2nd order (UNO2) scheme [22], which is adapted from the MINMOD scheme [35]. As the implicit diffusion of the 2nd order advection scheme is much smaller than that of the first order scheme, the diffusion term is simplified to be isotropic so the cross-term vanishes. Besides, the refraction and GCT term provides extra directional smoothing, which makes the total smoothing biased towards the transverse direction, similar to the original asymmetrical smoothing term.

The advection flux with the UNO2 scheme [22] and the diffusion flux with a central-space finite difference scheme for a u-face between the central and downstream cells are merged into a single flux, given by

$$\Delta F_x = (u\psi^* - D_x G_{DC}) l_u \Delta t \tag{9}$$

where ψ^* is the mid-flux value evaluated with the UNO2 scheme (see Eq. (6) in [22]), $G_{DC} = (\psi_D - \psi_C)/(x_D - x_C)$ is the gradient between the central and downstream cells, l_u is the u-face length and Δt is the sub-time step. Both the advection and diffusion schemes are of 2nd order accuracy. The diffusion coefficient, $D_x = D_y$, is specified by the spectral component propagation speed, directional bin width and a user input swell age parameter as the transverse diffusion coefficient D_{nn}

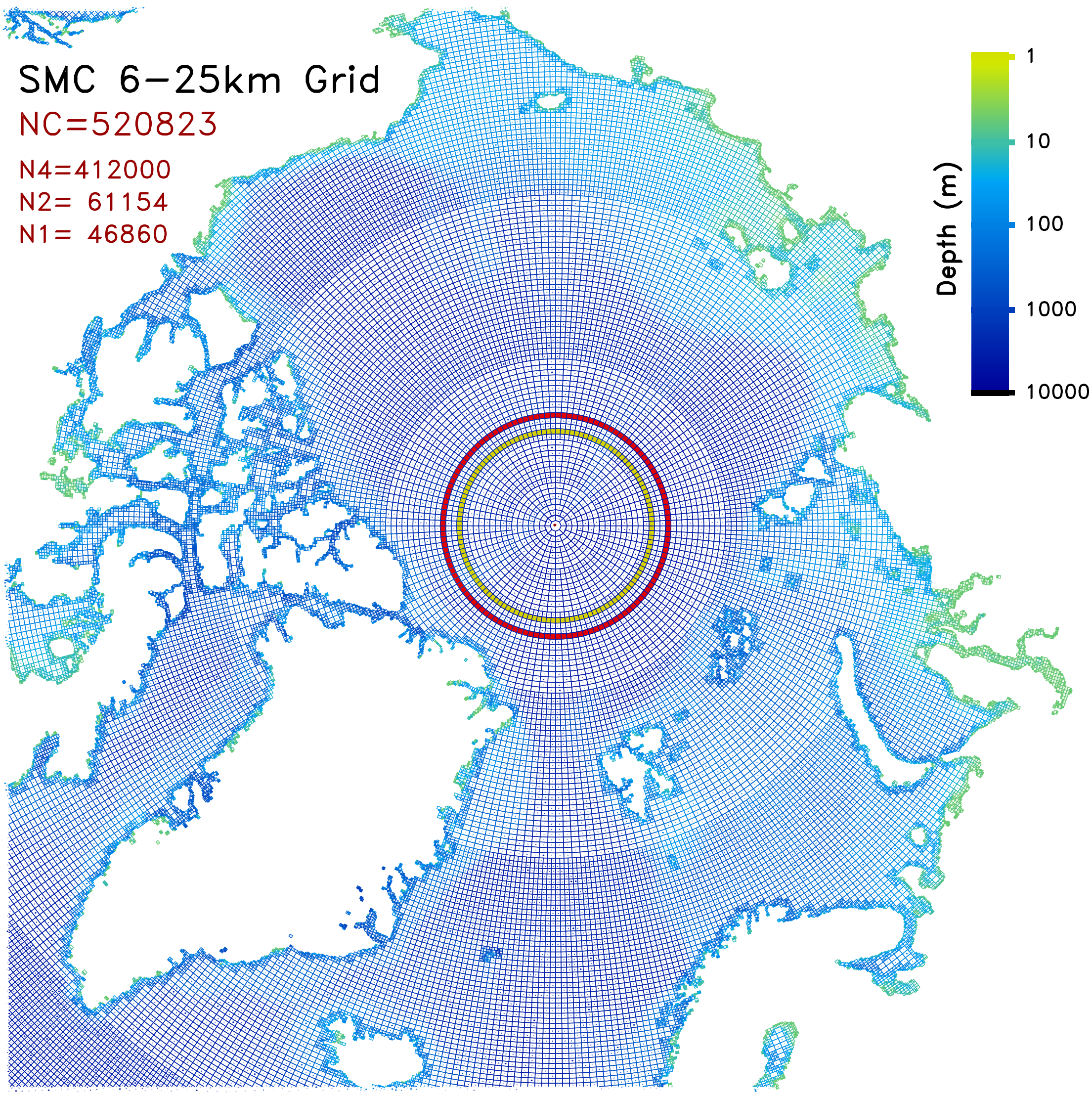

Fig. 2. The Arctic part of the spherical multiple-cell 6–25 km grid.

[4] in the original model. In the presence of an ambient ocean current, the wave energy propagation speed in the x-direction should be the sum of the group speed and current speed components, that is, $u = c_g \cos\theta + U_x$. As current effects on ocean surface waves are quite limited even in the Gulf Streams [15] or in a tidal river mouth [10], ocean current is not included in this study. The wave-current interaction may be important for some regions and will be included in the next stage, especially for regional models.

A temporary net-flux variable, F_{net}, is used for each cell to gather all fluxes into the cell before it is used for the cell value update. The flux (9) is added to the downstream cell net-flux variable and subtracted from the central cell net-flux variable at the same time for energy conservation. The use of face sizes and the net flux variables allow fluxes from different sized faces to be added up in proportion to their face sizes. After the face loop is completed, each cell value is updated in a cell loop by

$$\psi^{n+1} = \psi^n + F_{net}/(l_x l_y) \tag{10}$$

where $l_{x/y}$ is the cell x/y-length. The cell y-length is required for x-flux update to cancel the face length used in sum of the fluxes in proportion to the u-face length. The υ-face fluxes are calculated similarly except for the additional latitude cosine factor.

For the multi-resolution SMC6-25 grid, the face and cell loops are sorted into 3 sub-loops according to their y-sizes, thanks to the unstructured nature of the SMC grid. Advection-diffusion terms for the refined 6- and 12-km cells are calculated at ¼ and ½ of the base cell time step, that is, the 6-km flux and cell loops are done twice before the 12-km flux and cell loops are calculated once. The base level flux and cell loops are only calculated at each base cell time step. The temporary net-flux variable is used to accumulate fluxes between different levels and is reset to zero once it is used for its cell update. The simple loop-regrouping technique for multi-resolution SMC grid allows a smooth transfer from a single resolution SMC grid to a multi-resolution grid with optimised efficiency.

Another feature of the SMC grid is the unification of boundary conditions with internal flux evaluations. Cell faces at coastlines are assumed to be bounded by two consecutive empty cells. Thus, any wave energy transported into these empty cells will disappear, and no wave energy will be injected out of these zero cells into any sea cells. This convenient setup conforms to the zero wave energy boundary condition at land points used by ocean surface wave models and allows all the boundary cell faces to be treated in the same way as internal faces in one face loop. In addition, the periodic boundary condition for a global model is automatically included by the unstructured grid. So short boundary loops are avoided in the SMC grid propagation schemes and the full face and cell loops are streamlined for vectorization and parallelization.

An additional benefit of using two consecutive zero-boundary cells beyond the coastline is the complete blocking of wave energy by single-point islands. On a conventional lat–lon grid, wave energy can 'leak' through a single-point island due to the interpolation with neighbouring sea points in transport schemes which use a 5-point stencil like the UNO2 scheme. In the SMC grid, any single-point island is extended with two zero cells beyond its boundary face. As a result, wave energy cannot pass through such 'expanded island'. Nevertheless, sub-grid obstruction scheme from the original WAVEWATCH III model is kept to count for islands unresolved by the 6-km resolution. The sub-grid obstruction scheme follows the approach of Hardy et al [11] with some modifications [41].

The 2nd order explicit diffusion term is of the same order as the implicit diffusion of the first order upstream advection scheme and hence the combined 2nd order advection-diffusion flux (9) is equivalent to a first order upstream advection flux [22]. In fact, the first order upstream scheme is deliberately chosen in some wave models for its efficiency and to make use of its implicit diffusion for smoothing of the GSE [45,5,17]. However, the implicit diffusion of the first order upstream scheme is not up to the smoothing job because its implicit diffusivity vanishes in the transverse direction if the wave direction is along one axial direction, causing unrealistically long shadows behind small islands [49]. Although shifting component directions out of alignment with axial directions may avoid the long shadows, it could not alter the inherent nature of the implicit diffusion, including that it is larger in the propagation than the transverse direction and its diffusivity varies with the Courant number [22]. For regional models where long-distance propagation (and hence GSE smoothing) is not required, the first order upstream scheme is still a good choice because of its efficiency. For a global model it is considered too diffusive [39] because of its large diffusivity in the propagation direction even though its implicit diffusion is, sometimes, not enough for GSE smoothing. High order advection schemes then become the preferred choices for global wave model so that an explicit diffusion term can be included for the GSE smoothing. It is also convenient to make the diffusivity stronger in the transverse direction. The presence of the 2nd order explicit diffusion term, however, makes it unnecessary to use 3rd or higher order advection schemes in wave models because the diffusion term degrades all high order advection schemes to an equivalent first order scheme [22]. Using a 2nd order advection scheme then becomes the most optimised choice to maintain efficiency and to include an explicit diffusion term as in (1) for the GSE smoothing. The UNO2 scheme has been used in the Met Office operational wave models since 2006. Its performance is comparable to that using a 3rd order scheme [20] but saves about 30% of advection computation.

3.2. Refraction and spectral shift schemes

It should be emphasized that the linear surface wave theory is only valid when the water depth is non-zero [8]. When h approaches zero, for instance, the refraction rate (7b) becomes undefined because the ξ factor approaches infinity ($\xi \sim 0.5\sqrt{g/h}$). It is then customary in wave models to use a minimum water depth for the refraction term. A minimum water depth of 10 m is used in this comparison study and the refraction factor will be less than 0.5.

Apart from shallow water depth, steep ocean floor and large time step may also result in a large refraction rate. For instance, if the discrete depth gradient is assumed to be $\Delta h/\Delta x = 0.1$ and time step is $\Delta t = 1000$ s, the maximum refraction angle per time step might be $\Delta t \Delta h/2\Delta x \sim 50$ rad or about 8 full circles, which is no longer physically meaningful and is too large to fit into any advection-like refraction schemes used in contemporary wave models. One way to avoid this unrealistic large refraction increment is to use a small time step but this usually turns out to be too restrictive for wave models. Since refraction in a wave model is usually a minor process and is confined to coastal regions, the refraction increment is simply reduced to fit for the advection-like CFL condition in some wave models [45,5,42]. The CFL condition requires the refraction angle increment per time step to be less than one directional bin width (about 10°) and, of course, reduces the refraction effect. The latest version of the WAVEWATCH III model uses sub-time step to relax this restriction on the refraction term.

Here for the SMC grid wave model, a rotation scheme is substituted for the advection-like scheme to estimate the refraction term so that the CFL limit can be avoided. The rotation scheme is similar to a re-mapping advection scheme and is unconditionally stable. Although the rotation scheme does not have any limit on the refraction increment, the refraction angle should not pass beyond the depth gradient line (where $\mathbf{n} \cdot \nabla h = 0$) as stated in the refraction rate (7b). This physical limiter on the total refraction angle is included in the rotation scheme. The angle between the spectral direction and the depth decrease direction is calculated by:

$$\gamma = \cos^{-1}[-(h_x \cos\theta + h_y \sin\theta)/\sqrt{h_x^2 + h_y^2}] \tag{11}$$

where h_x and h_y are the water depth gradient along x and y axis, respectively. Because FORTRAN function ACOS returns value between 0 and π, the maximum refraction angle (absolute value) is then chosen to be less than $\pi/2$ with $\Delta\theta_{mxrfr} = \min(\eta,\ \gamma,\ \pi - \gamma)$. The constant η ($<\pi/2$) is a user-defined maximum refraction angle to reduce the refraction effect if required. If η is set to be less than one directional bin width, the rotation scheme will be equivalent to the original advection-like scheme in the WAVEWATCH III model without using sub time steps. For the present comparison study, the refraction limiter is set to be $\pi/3$. This refraction limiter may prevent all directional components from converging at the depth gradient direction within one time step, which may result in unrealistic large wave energy like caustics in ray tracing models [6,2]. It also creates room for merging the refraction with other directional changing terms, such as the refraction by ambient current and the GCT term.

The GCT term (8) can be fit into an advection-like scheme because it is usually less than one directional bin ($\sim$10°). For instance, if the time step is less than 900 s, the GCT angle (8) will be less than 1° per time step below 85° latitude, as the wave propagation angular speed, c_g/r, is on the order of 10^{-6} rad s^{-1}. However, as the refraction term is calculated with a rotation scheme in the SMC grid model, the GCT term is simply appended to the refraction term to form a total rotation angle. The rotation subroutine rotates each directional component by the combined angle and partitions its energy into the two directional bins which the rotated one strides across after the rotation. This simple rotation subroutine not only removes the time step restriction on the refraction angle but also adds an implicit diffusion in the θ direction because its implicit diffusivity is equivalent to that of the first order upstream scheme. This additional smoothing in the transverse direction is desirable for wave models to mitigate the GSE.

The spectral shift term, fourth in (1), is calculated with an advection-like UNO2 scheme in the k-space because the spectral shift is usually small enough to meet the CFL condition. The term is calculated at the base time step for all cell spectra.

3.3. The polar problem

The ocean surface wave energy spectrum is usually defined as discrete directional components from a reference direction at the local east and each directional component is assumed to be a scalar in wave propagation. This scalar assumption has been taken for granted in finite difference schemes, such as, calculation of the local gradient, $G_{DC} = (\psi_D - \psi_C)/(x_D - x_C)$, where the vector components ψ_D and ψ_C for the two neighbouring cells are assumed to be at the same direction, that is, to be treated as a scalar. This scalar assumption is a good approximation for a global wave model when the ice covered Arctic area is excluded. However, the scalar assumption becomes erroneous at high latitudes on a reduced grid since the change of direction over one grid-length grows too large to be ignored. For instance, in the SMC6-25 grid there are 8 cells immediately around the polar cell (see Fig. 2), the local east direction changes by 45° over one cell length. In some reduced grids where 4 triangle cells are used around the Pole, the situation is even worse because the local east direction changes 90° over one cell length and the velocity u and υ components are completely mixed up. This is why dynamical models based on finite-difference schemes on reduced grids are not satisfactory in the polar region as reviewed by Williamson [47]. Williamson also points out that this is not an issue with scalar variables, such as transport of tracers on reduced grid with finite-difference schemes [23]. It is also fine for semi-Lagrange methods, which transport the vector velocity rather than the components using trajectory on transformed coordinates near the poles [47]. Besides, the north polar cell does not have a local east direction, rendering the local east wave spectral definition impractical at the Pole. The invalid scalar assumption based on local east reference direction in the polar region prevents extension of ocean surface wave models at high latitudes.

This invalid scalar assumption problem in the reduced grid polar region can be avoided by switching to a fixed reference direction, for instance, the map-east direction as viewed on a stereographic projection of the polar region. Assuming the angle from the map-east to the local east is α, the wave spectral component for a given direction of angle θ from the local east will have an angle $\theta' = \theta + \alpha$ from the map-east. Its zonal and meridian group speed components are then given by

$$c_g \cos\theta = c_g \cos(\theta' - \alpha) \tag{12}$$

$$c_g \sin\theta = c_g \sin(\theta' - \alpha)$$

Note that the polar cell does not have a local east direction so the velocity could not be defined at the Pole as zonal and meridian components. In the SMC grid, however, only the meridian velocity component at the edge of the polar cell is required and there is no need to define the velocity at the polar cell centre [23]. This is one of the advantages of using a polar cell centred at the Pole. Nevertheless, velocity components at the Pole can be defined in the fixed reference system but they could not be converted into the local east system.

Because a given direction θ' from the map-east is constant in the Arctic region, the spectral component in the map-east system can be treated as a scalar for transport in the polar region. For the velocity in a dynamical model, its components along the map-east ($\theta' = 0$) and map-north ($\theta' = \pi/2$) can also be approximated as a scalar in the polar region. Their transport velocity components in the standard grid are then given by (12) after substituting their corresponding component values (u' and υ') for c_g, respectively. The polar cell can hold velocity or wave spectrum in the map-east system as scalars for transport but they do not need to be converted into the local east system.

This map-east direction can be conveniently approximated with a rotated grid with its rotated pole on the Equator. The standard polar region becomes part of the 'tropic region' in the rotated grid so the longitudinal direction of the rotated grid can be substituted for the map-east direction. For instance, if the rotated pole is at 180°E on the Equator, the angle α from this map-east to the local east at longitude λ and latitude φ within the Arctic region can be worked out with:

$$\alpha = \mathrm{sgn}(\cos\varphi\sin\lambda)\arccos\left[\frac{\cos\lambda\sin\varphi}{\sqrt{1-(\cos\lambda\cos\varphi)^2}}\right] \tag{13}$$

If the map-east is used within the Arctic region and local east in the rest for definition of the wave spectrum, there will be no fixed corresponding components between the two systems because α varies with longitude and latitude. For this reason, wave spectra defined by local east could not be mixed up with those defined from the map-east and the Arctic region using the map-east reference direction has to be separated from the rest which uses local east reference directions. In the SMC grid shown in Fig. 2, the reference direction change is set between the 3rd (at about 83°) and 4th (at 86.4°) size-changing parallels (see definition in [23]), where the local east direction changes less than 3° over one cell length as there are 128 cells in one row. The Arctic part and the rest (will be referred to as the *global part*) are linked together through 4 over-lapping rows. Wave spectra in the lower two of the 4 over-lapping rows in the Arctic part are updated with wave spectra from the global part after they are rotated anticlockwise by α. Wave spectra in the upper two rows of the 4 over-lapping rows in the global part are updated with wave spectra from the Arctic part after a clockwise rotation by α. Because of the unstructured nature of the SMC grid, the Arctic cells are appended behind the global part in the single cell list for propagation. The two parts can be conveniently separated by using sub-loops. The overlapping rows are treated in the same way as other cells so the propagation is calculated together for both parts. Wind direction and other direction related source terms have to be modified within the Arctic part to use the map-east reference direction.

If only the velocity components are dealt with within the Arctic (such as in a dynamic model), there is no need to work out the angle itself. The cosine and sine of the rotation angle will be enough for velocity conversion between the map-east and local east system. The rotation angle cosine and sine are given by

$$\cos\alpha = \frac{\cos\lambda\sin\varphi}{\sqrt{1-(\cos\lambda\cos\varphi)^2}}, \quad \sin\alpha = \frac{\sin\lambda}{\sqrt{1-(\cos\lambda\cos\varphi)^2}}, \tag{14}$$

The conversion between the map-east velocity components u' and v' and the local east velocity components u and v are given by

$$\begin{pmatrix} u' \\ v' \end{pmatrix} = \begin{pmatrix} \cos\alpha & -\sin\alpha \\ \sin\alpha & \cos\alpha \end{pmatrix}\begin{pmatrix} u \\ v \end{pmatrix}, \quad \begin{pmatrix} u \\ v \end{pmatrix} = \begin{pmatrix} \cos\alpha & \sin\alpha \\ -\sin\alpha & \cos\alpha \end{pmatrix}\begin{pmatrix} u' \\ v' \end{pmatrix} \tag{15}$$

That is, the local east velocity vector is rotated anticlockwise by the angle α as viewed in the map-east system. The wind component relationship (15) may also be used in the Arctic part to convert the local east wind to the map-east wind for wave model source terms.

4. Comparison of SMC and lat–lon grid models

4.1. Model configurations

Three model configurations are used for this comparison. The first configuration is the original global lat-lon grid at the base resolution of $\Delta\lambda$ = 360°/1024 = 0.3515625° and $\Delta\varphi$ = 180°/768 = 0.234375°, which will be referred to as the global 25 km (G25) model. Due to the polar restriction of the lat-lon grid, the Arctic above 82°N is not included in the G25 model domain. There are 688 rows and 482248 sea points in total, or about 68.5% of the total grid points (1024 × 688 = 704,512).

The second configuration is a single-resolution SMC grid, which is set to be identical to the G25 grid except that the SMC grid follows the merging rules at high latitudes as described in [23]. The north boundary is also at 82°N as in the G25 model. This SMC grid wave model will be referred to as the SMC25 model. The total cell number in SMC25 is reduced to 429,722, only about 61.0% of the full G25 lat–lon grid (704,512), after removing all land points and merging at high latitudes. The merging reduces the total cell number but does not reduce sea surface area. In fact, it increases sea surface area as some land points are turned into sea points if they are merged with sea points.

The third configuration is the SMC6-25 grid and the Arctic view of this SMC6-25 grid is shown in Fig. 2. The global part of the SMC6-25 grid has been extended to about 86°N or row 704 (the filled golden ring in Fig. 2[1]) so that it covers all open sea surfaces. The Arctic part started at row 701 (the filled red ring), with 4 overlapping rows (701–704) to provide the boundary cells for transition between the two reference direction zones. The SMC6-25 grid is produced from a 6 km bathymetry and is slightly different from the 25 km one. There are 520,823 cells in the SMC6-25 grid, including 46,860 finest cells at 6 km resolution and 61,154 cells at 12 km resolution but excluding the 4 overlapping rows. The total number of sea points is larger than the number of G25 sea points (482,248) due to the refined resolutions.

All the three models share the same sourcing terms and the 25 km surface wind forcing. Model time covers over 3 months from 20 July 2010 to 31 October 2010 and one month, 20100901-30, is used for the comparison. September coincides with

[1] For interpretation of color in Fig. 2, the reader is referred to the web version of this article.

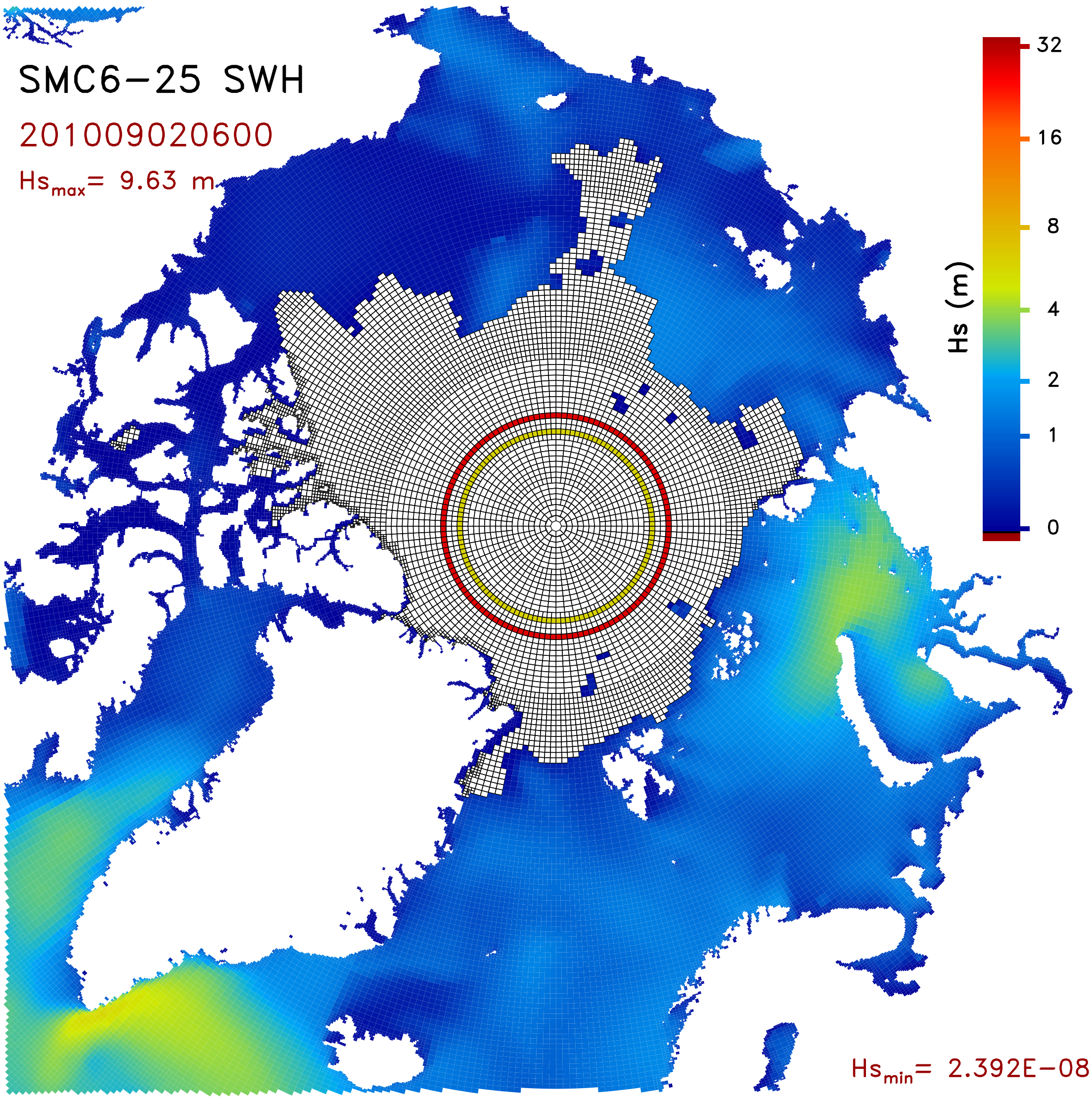

Fig. 3. SMC6-25 model SWH field in the Arctic on 2 September 2010.

the annual minimum of Arctic sea ice coverage and allows the open sea latitudes as high as possible. Fig. 3 shows the SMC6-25 model significant wave height (SWH) field on 2 September 2010 when the sea ice coverage in the Arctic is close to its annual minimum. The highest latitude of the Arctic sea ice edge reached about 83°N in 2010, just beyond the north boundary of the G25 model but inside the global part of the SMC6-25 grid. So the Arctic part in the SMC6-25 model (above 86°N) is completely covered by sea ice during the study period and is not activated in this study. The Arctic part is used in an ice-free wave spectral propagation test to demonstrate the map-east reference direction method.

All the three wave models are validated with SWH observations from the radar altimeter (RA2) on board the European Space Agency (ESA) Envisat satellite and buoy wave spectra from the USA National Data Buoy Centre (NDBC). The satellite SWH data are collocated with interpolated model values to minimise modification of the satellite data. This allows extra filters to be applied on the satellite data if required. For instance, spurious large satellite SWH values near coastlines pass through the ESA recommended filters but can be filtered out by comparing them to the interpolated model values [25]. Averaging the satellite data within model grid cell would make this kind of filter impractical. Full 2-D model spectra are saved at 40 spectral buoy sites but only 33 spectral buoys are active during the study period. Fig. 4 shows the SMC6-25 model SWH global field on 29 September 2010 and the 33 buoy locations marked by red dots below the 'Y' symbols.

4.2. Computing cost

Some key statistics of the three models are compared in Table 1. The models are run on an IBM Power 6 supercomputer in two modes, a 1-day hind-cast run using 1 node (32 CPUs or 64 cores) and a 5.5-day forecast run on 4 nodes (128 CPUs). As

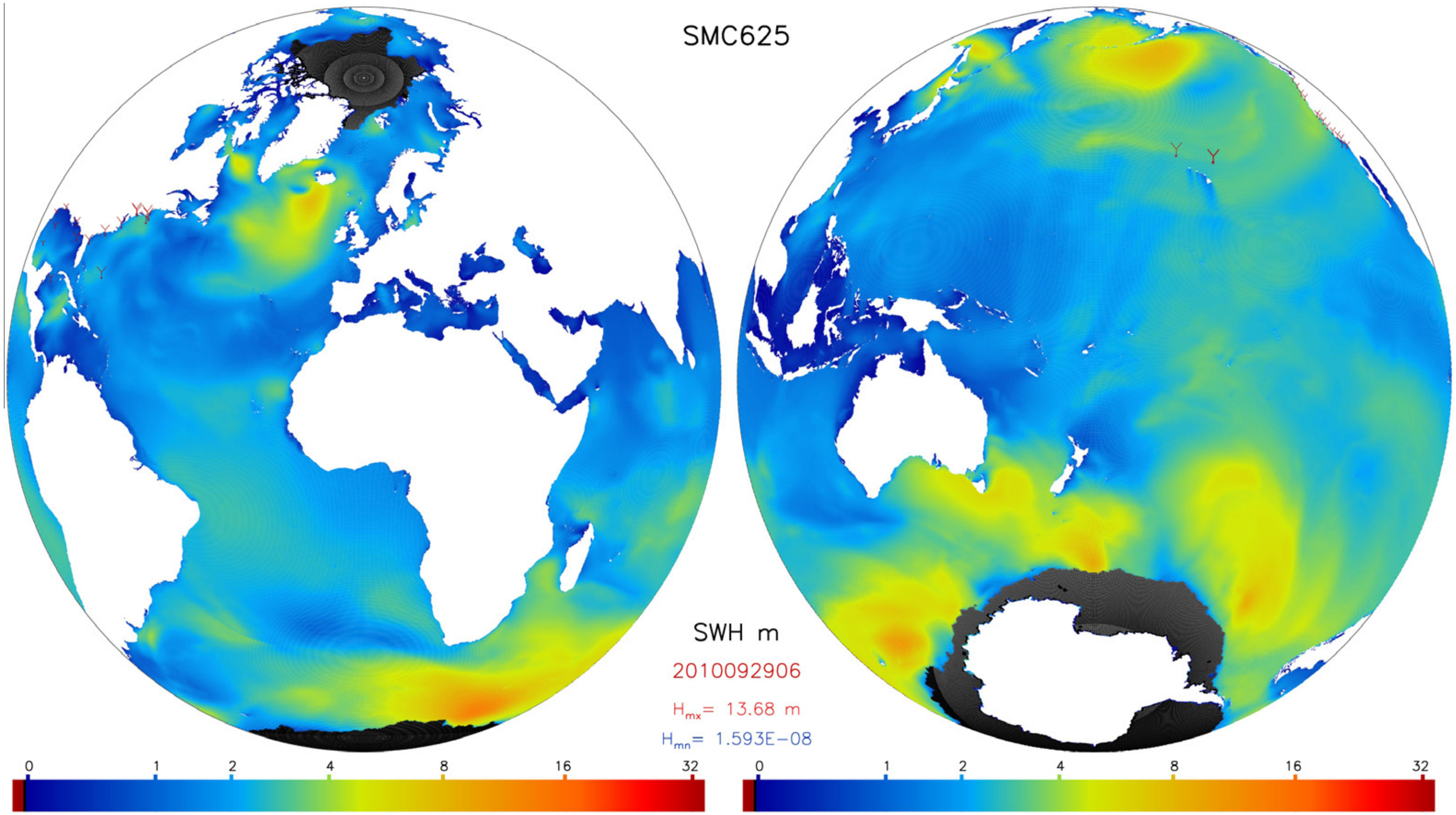

Fig. 4. SMC6-25 model global SWH field on 29 September 2010 with spectral buoys marked with 'Y' symbols.

Table 1
Comparison of the G25, SMC25 and SMC6-26 models. The percentages in parenthesis are relative to the G25 model values.

	G25	SMC25	SMC6-25
Number of grid (sea) points	704,512 (482,248)	429,722 (61%)	520,823 (74%)
Min advection time step (s)	180	600	600/300/150
1-D 1-node 64-Core (s/task)	330	202 (61%)	336 (102%)
5.5-D 4-node 128-C (s/task)	1800	1240 (69%)	1860 (103%)
No. RA2 – Model pairs	691,571	707,419 (102%)	704,615 (102%)
RA2 mean SWH/Stdv (m)	2.57/1.44	2.60/1.46	2.60/1.46
Model (RA2) SWH/Stdv (m)	2.70/1.49	2.68/1.49	2.66/1.49
Model – RA2 Stdv (m)	0.542	0.553	0.546
Model – RA2 correlation	0.933	0.931	0.932
No. buoy – Model pairs	23 064	23 064	23 064
Buoy mean SWH/Stdv (m)	1.37/0.836	1.37/0.836	1.37/0.836
Model (buoy) SWH/Stdv (m)	1.37/0.789	1.37/0.804	1.36/0.805
Model – buoy Stdv (m)	0.315	0.335	0.312
Model – buoy correlation	0.927	0.917	0.928

wave group speed changes with wave frequency, propagation time steps are maximised according to different spectral components. A minimum propagation time step is specified for the maximum group speed over the smallest grid length. The merged cells at high latitudes on the SMC grid allow the minimum time step to be increased by 4 times of the G25 model one (up to 82°N). The increase will be even more significant if the northern boundary is moved further up towards the Pole. The minimum propagation time step is 180 s for the G25 model and 600 s for the SMC25. Note that the SMC grid minimum advection time step (600 s) is not exactly 4 times of the G25 one (180 s) because it has to be an integer factor of the main time step (1800 s). The SMC6-25 model uses the same 600 s minimum time step for propagation over the base-level (25 km) cells but reduced sub-time steps (300 and 150 s) for the refined (12 and 6 km) cells. The increased propagation time step is the major advantage of the SMC grid over the lat–lon grid.

Removing land points out of the propagation scheme also helps in reduction of cost. Because the SMC grid propagation scheme is framed on sea points only, there is no need to convert sea points to the full grid and vice versa. Besides, propagation scheme on the SMC grid does not need boundary conditions so the propagation loops are streamlined for vectorization and parallelization. The source terms are calculated on sea points only at the same main time step (1800 s) for all three models. Because SMC25 cell number (429,722) is about 89% of the G25 sea points (482,248), SMC25 may save 11% on source term. The combined effects lead to a total CPU time reduction by about 1/3 on the SMC25 grid in comparison with that on the G25 grid as shown in Table 1.

For the SMC6-25 grid, the SMC25 grid saving is cancelled by the refined resolutions. Note that propagation over refined cells are calculated at sub-time steps, each 6 km cell is equivalent to 4 base-level (25 km) cells in transport calculation and each 12 km cell costs as 2 base-level (25 km) cells. So the effective cell number in the SMC6-25 grid is $412{,}000 + 2 \times 61{,}154 + 4 \times 46{,}860 = 721{,}748$, which is even larger than the full G25 grid number (704,512). It is then not a surprise that the CPU time of the SMC6-25 model is longer than the G25 one as shown in Table 1. Nevertheless, the SMC6-25 model still has the advantage of increased advection time step. However, source term cost for the SMC6-25 is increased due to the increased sea points ($520{,}823/482{,}248 \sim 1.1$). Detaching the Arctic part from the propagation has very little contribution towards cost reduction because it has only 1321 base-level cells, including 512 boundary cells. Note that the SMC6-25 global part covers up to 86°N, higher than the G25 grid (82°N). If the G25 lat-lon grid model was extended to 86°N, its minimum advection time step would, at least, have to be halved to 90 s.

These timing tests indicate that the SMC grid can reduce the overall CPU consumption of the global wave model by about 1/3 in comparison with the original lat–lon grid. This huge reduction in computation cost is highly desirable for operational models and creates rooms for spatial resolution increase and source term upgrades. Besides, the SMC global part can be extended conveniently to high latitudes (86°N in SMC6-25) without reducing the advection time step. This will be enough to cover the open space in the Arctic summers so far without the complication of two reference direction zones, which will be required when high latitudes above 86°N have to be included in the future.

4.3. Comparison with observations

Predicted SWH fields from the three models are compared with altimeter and buoy observations, respectively, and their statistics are also listed in Table 1. Over the one month (September 2010) study period, there are 691,571 altimeter entries passed the quality control and paired with interpolated SWH values from the G25 model. The interpolation is among model grids and between model time steps. The mean SWH of these 691,571 RA2 observations is 2.57 m with a standard deviation (Stdv) of 1.44 m. The mean SWH and Stdv from the corresponding G25 model interpolations are 2.70 and 1.49 m, respectively. The Stdv of the SWH differences between the G25 model and the RA2 data is 0.542 m. Their correlation coefficient is 0.933.

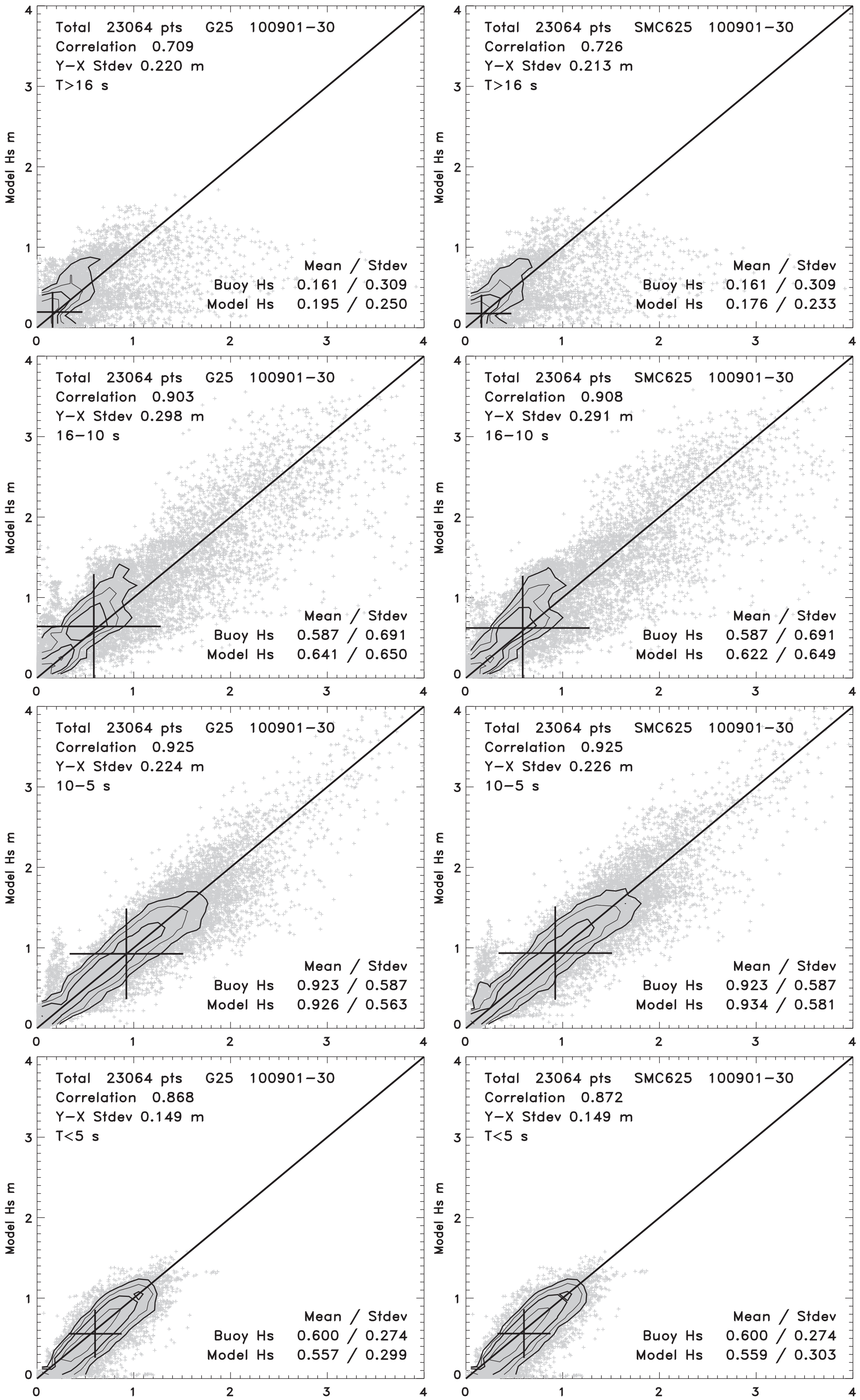

Fig. 5. Comparison of G25 (left column) and SMC6-25 (right column) wave model 4-bin SRWH with September 2010 spectral buoy data.

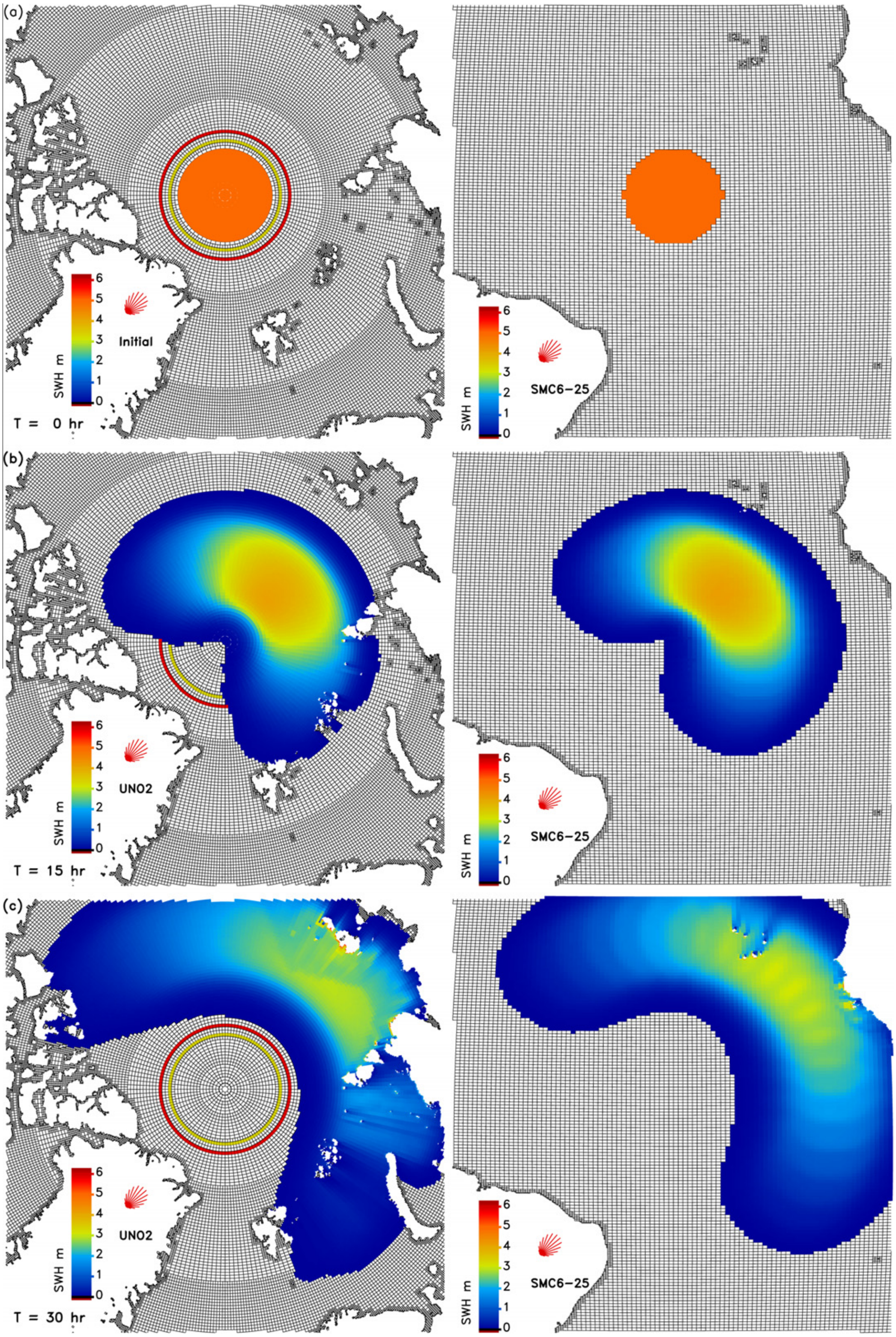

Fig. 6. Comparison of the wave spectral propagation using Arctic map-east (left column) and the conversional local east (right column) reference direction methods.

The SMC models are validated against the RA2 data in a similar way and the results are listed beside the G25 ones in Table 1. The SMC model output is first converted onto the standard lat–lon grid. From there they share the same collocation procedure with the G25 model validation. However, as the SMC sea surface area is slightly larger than the G25 one, the numbers of RA2 entries selected for both SMC models are larger than the G25 one. So most of the extra entries (15,848 for SMC25 and 13,044 for SMC6-25) come from coastal regions. Because altimeter SWH is spuriously too large in coastal regions due to radar echo contaminations by land surfaces, the extra coastal points have negative impact on the statistics. Note that the Arctic ice-line is below 83°N in the study period, the extended Arctic region in the SMC6-25 model does not bring in extra RA2 data. In fact the total RA2 entries for the SMC6-25 model (704,615) is smaller than the SMC25 one (707,419) because SMC6-25 has resolved more land surface than SMC25. The extra coastal RA2 high values are revealed by scatter plots and are also reflected by the increased RA2 mean SWH value (2.60 m via the G25 one 2.57 m). The SMC mean SWH values (2.68 and 2.66 m) are closer to the RA2 one (2.60 m) than the G25 model value (2.70 m).

The Stdv of the SWH differences between each SMC model and the RA2 data is comparable with the G25 one and so is the correlation coefficient. The SMC25 model performs slightly less than the other two models with increased Stdv (0.553 m) and reduced correlation (0.931). The increased error in the SMC25 model is attributed partially to the increase of coastal points in the collocated data. The increased temporal truncation error due to increased time step (from 180 s for the G25 model to 600 s for the SMC25 model) and reduced spatial resolution at high latitudes due to cell merging in the SMC grid are also possible reasons for the increased error. This small increase in error may be considered the price for the large reduction in computing cost.

The three models are also validated against 33 spectral buoy observations in the study period and the results are also listed in Table 1. The spectral buoy positions are shown in Fig. 4 by the red dots below their 'Y' marks. All three models share the same data set so they have the same number of collocations (23,064). The buoy results are consistent with those of the altimeter data comparison, that is, the G25 and SMC6-25 models are better than the SMC25 model. The buoy data indicate that the SMC6-25 model is the best among the three models with the smallest error (0.312 m) and the highest correlation (0.928). Most of the buoys are close to the US coastlines so they are quite sensitive to coastal resolutions. This is the main reason why the SMC6-25 model stands out. In fact, the refined coastal resolutions make the coastal blocking effect more accurate in SMC6-25 than in the other two models. This coastal blocking effect is visible in Fig. 4, particularly around the Canary Islands in the Atlantic and the Hawaii Islands in the Pacific.

The refined coastal resolution improves prediction of long distance swells. All coastlines are physical sinks to wave energy and all islands in swell paths leave some dents on the passing waves. This improvement is revealed by comparing the spectral performance of the G25 and SMC6-25 models in Fig. 5 with the help of a 4-bin sub-range wave height (SRWH), which is defined in analogue to the SWH but integrated over a limited frequency range [25]. The 4-bin margins are marked with wave period $T > 16$ s, 16-10 s, 10-5 s and $T < 5$ s, respectively. The SRWH values integrated from the spectra of the 33 buoys are compared with the corresponding values from the two models, respectively. The 4 panels in the left column are the 4-bin SRWH scatter plots for the G25 model against the 33 buoys and the right column are for the SMC6-25. The 10-5 s and T < 5 s bins may be considered to be locally generated wind sea and independent of transport. As the two models use exactly the same source terms, the wind sea is almost identical as compared with the buoy wind sea. The $T > 16$ s and 16-10 s bins may be considered to be the long-distance swell field, which should bear the islands blocking dents when they arrive at the coastal buoy sites. The SMC6-25 model is clearly better than the G25 model in agreement with the buoy swell observations, confirming that the blocking effect is better represented in SMC6-25 than in G25.

5. Map-east method in the Arctic

The proposed map-east direction method in the Arctic could not be tested in the wave model against observations because the polar region is still covered by sea ice all year round. An idealised wave propagation test on the SMC6-25 grid in an ice-free Arctic is used here for demonstration. The test includes all the 4 terms (advection, diffusion, refraction and GCT) in (1) but does not have any source term. The transient zone from the global to the Arctic parts is around 86°N and the map-east reference direction is used within the Arctic part (area within the red ring in Fig. 2). A constant wave spectrum is assigned to all cells within a 3.75° radius from the N Pole. The wave spectrum has 36 directions and a fixed frequency at 0.0625 Hz or period $T = 16$ s. Because all frequencies show the same directional pattern, one frequency is sufficient for this demonstration. The initial wave spectrum is defined by

$$E(\theta) = \begin{cases} E_0 \cos^2(\theta - \theta_p), & \text{for } |\theta - \theta_p| < \pi/2 \\ 0, & \text{Otherwise} \end{cases} \tag{16}$$

where $E_0 = 50/\pi$ is a constant, θ_p is the peak direction. The transported spectrum is integrated as the wave height, $H = \sqrt{\int E d\theta}$, similar to the SWH used in wave models apart from a constant factor.

To assess the map-east method, another round patch of the same size as the Arctic one is initialised in the Atlantic close to the Equator (centred at 33°W 5°N). As long as the two patches share similar propagation pattern, the map-east method may be considered to be equivalent to the local east method. Because the local east method is validated with observations, the comparison may be considered as an indirect validation of the map-east method against observations. The two round patches are drawn side by side in Fig. 6 for this comparison. All other cells are initialised to be zero. The gravity depth is about 64 m for the given frequency (0.0625 Hz) ocean surface wave and its group speed is about 12.5 m s^{-1} in deep waters. The time step is 300 s for the smallest (6 km) cells and is increased to 600 and 1200 s for the 12 km and 25 km cells, respectively, resulting in a maximum Courant number of 0.929.

The two initial round patches are shown in row (a) of Fig. 6 and the non-zero wave height is constant 5 units. Because of the different shapes of the grid cells at the two sites, the Arctic patch has a round edge while the Atlantic patch has a stepped edge. Nevertheless, the two patches cover approximately the same area. The two co-centred rings in the Arctic plots mark the transient zone from the local east to the map-east reference directions. The initial spectral peak direction θ_p is 45° from their reference direction, respectively, as indicated by the spectral roses in Fig. 6. Because the Arctic part uses a fixed map-east reference direction, the initial spectral peak direction is constant within the Arctic part. In the global part, however, the local east reference direction changes with longitude and so the peak direction of the initial spectrum. This is why the Atlantic round patch is initialised near the Equator to minimise the local direction change.

The middle row (b) of Fig. 6 shows the two patches after 15 hrs of propagation. The centre of the Arctic patch has covered the transient zone. It is evident that there is no visible interruption of the patch distribution in the two reference direction parts. The Arctic patch is quite similar to the Atlantic one shown on the right side except for the fine cuttings caused by local islands. The bottom row (c) of Fig. 6 shows the two patches after 30 hrs when the Arctic patch is out of the map-east zone. The two patches still share a quite close distribution in the deep waters. The blocking effects by local islands and water depth induced refraction and speed changes have left their unique marks on the two patches. These results confirm that the map-east method is effective for wave spectral propagation in the polar region and solved the polar problem in finite difference schemes on reduced grids. The transition between the two reference direction zones is smooth and does not cause any visible interruptions in surface wave spectral propagation.

6. Summary and conclusions

A SMC grid [23] has been installed in the Met Office global wave model, which is adapted from the WAVEWATCH III model [38,43]. The SMC grid relaxes the CFL restriction at high latitudes by merging the longitudinal cells and removes the polar singularity by introducing a round polar cell. The unstructured SMC grid allows all land cells to be removed out of wave propagation schemes. The time step relaxation and land cell removal result in an overall computation time reduction by about 1/3 in comparison with the original latitude–longitude grid model. The SMC grid permits variable spatial resolutions within one model domain so that coastlines and small islands can be resolved at refined resolutions while the open ocean is kept in affordable resolution. The multi-resolution feature also makes it possible to merge regional models into a single global model, replacing nested models in operational forecasting systems.

A 2nd order upstream non-oscillatory (UNO2) scheme [22] is used for the advection term, combined with a centre-in-space 2nd order scheme for the diffusion term. A rotation scheme is used for wave spectral refraction and GCT to avoid the CFL restriction of the advection style schemes used for these terms in the original model. The rotation scheme provides extra smoothing in the transverse direction to suppress the GSE. Validations with satellite and buoy observations show that the SMC grid wave model performs as well as the lat–lon grid model. Swell prediction is improved if small islands and coastal features are resolved with refined resolutions in the SMC grid.

A map-east reference direction method is introduced to tackle the polar problem with vector component propagation near the Pole. The map-east is substituted for the local east in the polar region to define wave spectrum so that the scalar assumption can be maintained. This method makes it possible to expand global wave models to cover the whole Arctic in response to the Arctic sea ice retreat in future summers. Ocean surface wave spectral energy propagation in an ice-free Arctic is demonstrated to illustrate the map-east method. An indirect validation is facilitated by comparing the Arctic propagation with a similar propagation pattern near the Equator because direct validation with observations is not practical in the Arctic due to its ice coverage. The comparison indicates that the map-east method is effective for wave spectral propagation in the Arctic and solves the polar problem for vector component advection on reduced grids with finite difference schemes.

Acknowledgements

The author is grateful to the editor and the three anonymous reviewers for their useful comments and suggestions. The author would also like to thank other wave modellers, particularly Dr Hendrik Tolman (NOAA), for discussions on some technical details.

References

[1] F. Ardhuin, T.H.C. Herbers, Numerical and physical diffusion: can wave prediction models resolve directional spread?, J Atmos. Oceanic Technol. 22 (2005) 886–895.
[2] F. Ardhuin, T.H.C. Herbers, W.C. O'Reilly, A hybrid Eulerian-Lagrangian model for spectral wave evolution with application to bottom friction on the continental shelf, J. Phys. Oceanogr. 31 (2001) 1498–1516.
[3] J.A. Battjes, Refraction of water waves, J. Waterways and Harbors Division, ASCE, WW4, 1968, pp. 437–451.
[4] N. Booij, L.H. Holthuijsen, Propagation of ocean waves in discrete spectral wave models, J. Comput. Phys. 68 (1987) 307–326.
[5] N. Booij, R.C. Ris, L.H. Holthuijsen, A third-generation wave model for coastal regions. 1. Model description and validation, J. Geophys. Res. 104 (C4) (1999) 7649–7666.
[6] L. Cavaleri, P. Malanotte-Rizzoli, Wind-wave prediction in shallow water: theory and applications, J. Geophys. Res. 86 (1981) 10961–10973.

[7] A. Chawla, H.L. Tolman, Obstruction grids for spectral wave models, Ocean Model. 22 (2008) 12–25.
[8] J. Falnes, Ocean Waves and Oscillating Systems, Cambridge University Press, Cambridge, UK, 2002. 275 pp.
[9] C. Guan, H. Ju, Empirical formula for wave length of ocean wave in finite depth water, Chin. J. Ocean. Limno. 23 (2005) 17–21.
[10] C. Guan, V. Rey, P. Forget, Improvement of the WAM wave model and its application to the Rhone River Mouth area, J. Coastal Res. 15 (1999) 966–973.
[11] T.A. Hardy, L.B. Mason, J.D. McConochie, A wave model for the Great Barrier Reef, Ocean Eng. 28 (2000) 45–70.
[12] S. Hasselmann, K. Hasselmann, J.H. Allender, T.P. Barnett, Computations and parameterizations of the nonlinear energy transfer in a gravity-wave spectrum. Part II: Parameterizations of the nonlinear energy transfer for application in wave models, J. Phys. Ocean. 15 (1985) 1378–1391.
[13] L.H. Holthuijsen, Waves in Oceanic and Coastal Waters, Cambridge Univ. Press, Cambridge, UK, 2007. 387 pp.
[14] L.H. Holthuijsen, A. Herman, N. Booij, Phase-decoupled refraction-diffraction for spectral wave models, Coastal Eng. 49 (2003) 291–305.
[15] L.H. Holthuijsen, H.L. Tolman, Effects of the Gulf Stream on ocean waves, J. Geophys. Res. 96 (C7) (1991) 12755–12771.
[16] P.A.E.M. Janssen, The Interaction of Ocean Waves and Wind, Cambridge University Press, Cambridge, UK, 2004. 300 pp.
[17] P.A.E.M. Janssen, Progress in ocean wave forecasting, J. Comput. Phys. 227 (2008) 3572–3594.
[18] P.D. Killworth, J.G. Li, D. Smeed, On the efficiency of statistical assimilation techniques in the presence of model and data error, J. Geophys. Res. 108 (C4) (2003) 1–12. 3113.
[19] B. Kinsman, Wind Waves, their Generation and Propagation on the Ocean Surface, Dover Pub., New York, 1984. 676 pp.
[20] B.P. Leonard, The ULTIMATE conservative difference scheme applied to unsteady one-dimensional advection, Comput. Methods Appl. Mech. Eng. 88 (1991) 17–74.
[21] J.G. Li, A multiple-cell flat-level model for atmospheric tracer dispersion over complex terrain, Boundary-Layer Meteorol. 107 (2003) 289–322.
[22] J.G. Li, Upstream non-oscillatory advection schemes, Mon. Weather Rev. 136 (2008) 4709–4729.
[23] J.G. Li, Global transport on a spherical multiple-cell grid, Mon. Weather Rev. 139 (2011) 1536–1555.
[24] J.G. Li, B.W. Atkinson, An inert tracer dispersion scheme for use in a mesoscale atmospheric model, Atmos. Environ. 34 (2000) 4011–4018.
[25] J.G. Li, M. Holt, Comparison of ENVISAT ASAR ocean wave spectra with buoys and altimeter data via a wave model, J. Atmos. Oceanic Technol. 26 (2009) 593–614.
[26] M.S. Longuet-Higgins, On the transformation of a continuous spectrum by refraction, Proc. Cambridge Philos. Soc. 53 (1957) 226–229.
[27] R. Magne, K.A. Belibassakis, T.H.C. Herbers, F. Ardhuin, W.C. O'Reilly, V. Rey (Evolution of surface gravity waves over a submarine canyon), J. Geophys. Res. 112 (2007) C01002. 12 pp.
[28] W.H. Munk, M.A. Traylor, Refraction of ocean waves: a process linking underwater topography to beach erosion, J. Geol. 55 (1947) 1–26.
[29] R.D. Nair, B. Machenhauer, The mass-conservative cell-integrated semi-Lagrangian advection scheme on the sphere, Mon. Weather Rev. 130 (2002) 649–667.
[30] O.M. Phillips, The Dynamics of the Upper Ocean, second ed., Cambridge Univ. Press, Cambridge, UK, 1977. 336 pp.
[31] R.A. Pielke, Mesoscale Meteorological Modeling, Academic Press, Orlando, 1984. 612 pp.
[32] I.V. Polyakov, L.A. Timokhov, V.A. Alexeev, S. Bacon, I.A. Dmitrenko, L. Fortier, I.W. Frolov, J.C. Gascard, E. Hansen, V.V. Ivanov, S. Laxon, C. Mauritzen, D. Perovich, K. Shimada, H.L. Simmons, V.T. Sokolov, M. Steele, J. Toole, Arctic ocean warming contributes to reduced polar ice cap, J. Phys. Oceanogr. 40 (2010) 2743–2756.
[33] S. Popinet, R.M. Gorman, G.J. Rickard, H.L. Tolman, A quadtree-adaptive spectral wave model, Ocean Model. 34 (2010) 36–49.
[34] P.J. Rasch, Conservative shape-preserving two-dimensional transport on a spherical reduced grid, Mon. Weather. Rev. 122 (1994) 1337–1350.
[35] P.L. Roe (Large scale computations in fluid mechanics), in: E. Engquist, S. Osher, R.J.C. Sommerville (Eds.), Lectures in Applied Mathematics 22 (1985) 163–193.
[36] W.E. Rogers, T.J. Campbell, Implementation of Curvilinear Coordinate System in the WAVEWATCH III Model. *NRL Report* (2009) NRL/MR/7320–09-9193. http://www7320.nrlssc.navy.mil/pubs/2009/rogers1-2009.pdf.
[37] A. Roland, A. Cucco, C. Ferrarin, T.-W. Hsu, J.-M. Liau, S.-H. Ou, G. Umgiesser, U. Zanke, On the development and verification of a 2-D coupled wave-current model on unstructured meshes, J. Marine Sys. 78 (2009) S244–S254.
[38] H.L. Tolman, A third-generation model for wind waves on slowly varying unsteady and inhomogeneous depths and currents, J. Phys. Oceanogr. 21 (1991) 782–792.
[39] H.T. Tolman, Effects of numerics on the physics in a third-generation wind-wave model, J. Phys. Oceanogr. 22 (1992) 1095–1111.
[40] H.L. Tolman, Alleviating the Garden Sprinkler effect in wind wave models, Ocean Model. 4 (2002) 269–289.
[41] H.L. Tolman, Treatment of unresolved islands and ice in wind wave models, Ocean Model. 5 (2003) 219–231.
[42] H.L. Tolman, A mosaic approach to wind wave modeling, Ocean Model. 25 (2008) 35–47.
[43] H.L. Tolman, B. Balasubramaniyan, L.D. Burroughs, D.V. Chalikov, Y.Y. Chao, H.S. Chen, V.M. Gerald, Development and implementation of wind-generated ocean surface wave models at NCEP, Weather Forecast. 17 (2002) 311–333.
[44] H.L. Tolman, D. Chalikov, Source terms in a third-generation wind-wave model, J. Phys. Oceanogr. 26 (1996) 2497–2518.
[45] WAMDI group, The WAM model - a third generation ocean wave prediction model, J. Phys. Oceanogr. 18 (1988) 1775–1810.
[46] M. Wang, J.E. Overland, A sea ice free summer Arctic within 30 years?, Geophys Res. Lett. 36 (2009) L07502. 5 pp.
[47] D.L. Williamson, The evolution of dynamical cores for global atmospheric models, J. Meteorol. Soc. Jpn. 85B (2007) 241–269.
[48] D.L. Williamson, J.B. Drake, J.J. Hack, R. Jakob, P.N. Swarztrauber, A standard test set for numerical approximations to the shallow-water equations in spherical geometry, J. Comput. Phys. 102 (1992) 221–224.
[49] WISE Group, L. Cavaleri, J.-H.G.M. Alves, F. Ardhuin, A. Babanin, M. Banner, K. Belibassakis, M. Benoit, M Donelan, J. Groeneweg, T.H.C. Herbers, P. Hwang, P.A.E.M. Janssen, T. Janssen, I.V. Lavrenov, R. Magne, J. Monbaliu, M. Onorato, V. Polnikov, D. Resio, W.E. Rogers, A. Sheremet, J. McKee Smith, H.L. Tolman, G. van Vledder, J. Wolf, I. Young, Wave modelling – the state of the art. Progress Oceanogr. 75 (2007) 603–674.
[50] J. Zhang, R. Lindsay, M. Steele, A. Schweiger (What drove the dramatic retreat of arctic sea ice during summer 2007?), Geophys Res. Lett. 35 (2008) L11505. 5 pp.